CHEMISTRY OF MATERIALS

pubs.acs.org/cm

Article

Impact of Low-Temperature Seed-Assisted Growth on the Structural and Optoelectronic Properties of $MAPbBr_3$ Single Crystals

Published as part of the Chemistry of Materials virtual special issue "In Honor of Prof. Elsa Reichmanis".

Waqas Zia, Clara A. Aranda,* Jan Pospisil, Alexander Kovalenko, Monika Rai, Cristina Momblona, Setatira Gorji, Guillermo Muñoz-Matutano, and Michael Saliba*

Cite This: *Chem. Mater.* 2023, 35, 5458–5467

Read Online

ACCESS | Metrics & More | Article Recommendations | Supporting Information

ABSTRACT: This work presents a detailed investigation of seed and nucleation-assisted growth methods for the inverse temperature crystallization (ITC) of methylammonium lead bromide single crystals. We have demonstrated that low-temperature seed-assisted growth results in significant improvements in both optical and electrical responses of the material compared to the nucleation-assisted growth. Specifically, the space charge limited current method reveals a reduced trap-filled limit voltage of 0.287 V for the seed-assisted crystal compared to 0.923 V for the nucleation-assisted one, resulting in differences in trap density values. Temperature dependence space charge limited current analysis confirms these results, showing trap densities of 9.47×10^9 cm^{-3} for seeded crystal growth compared to 3.21×10^{10} cm^{-3} for the nucleation-assisted growth, as well as a lower trap energy level for the seeded crystal. The study also highlights that the low-temperature seed-assisted growth has a positive impact on the optical and crystalline properties of the material with improved photoluminescence response and a lower lattice strain determined by X-ray diffraction. Furthermore, the study demonstrates that this improved crystallization method has a significant influence on the photodetector properties of the crystal, leading to higher detectivity and responsivity values for the seed-assisted approach.

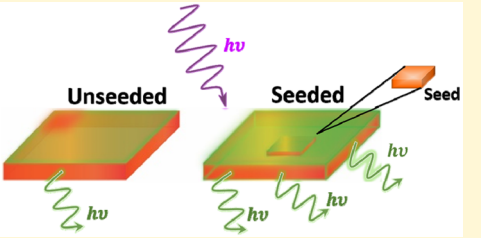

1. INTRODUCTION

Organic lead halide perovskites have skyrocketed in the photovoltaic field in the past decade. The high performance of perovskite solar cells,[1,2] light-emitting diodes,[3] and photodetectors[4] is based on their tunable optical, charge transport, and high absorption properties.[5] The most extensive research with perovskite materials has been performed on polycrystalline thin films. However, the grain-boundary free perovskite single crystals hold superior optoelectronic properties due to their lower trap densities and longer diffusion lengths.[6,7] These single crystalline perovskites can be used in numerous applications, such as electronic eyes,[8] image sensing in the medical field,[9] or photonic synapses.[10]

Apart from the excellent optoelectronic properties of Pb-based perovskite single crystals, numerous works are being performed to grow Pb-free perovskite single crystals to address the issues of sustainability and toxicity.[11] Sn-based perovskite single crystalline photodetectors have been employed for narrow bandgap photodetection[12] and NIR imaging.[13] Various shape control techniques to achieve single-crystalline thin films or nano/micro rods have also been developed to integrate the perovskite single crystals efficiently in the final optoelectronic devices.[14] However, in each case, sufficient quality of the perovskite single crystals is necessary.

Unfortunately, the crystalline growth process to obtain high-quality single crystals can be hard to control. Numerous growth techniques have been developed to obtain the optimum crystal properties for each application, e.g., solution temperature lowering (STL),[15] antisolvent vapor-assisted crystallization (AVC),[16,17] slow evaporation (SE),[17] and inverse temperature crystallization (ITC)[18] methods. Among them, the ITC (first introduced by Saidaminov et al.) is one of the most used growth methods. It is a nucleation-assisted growth process based on the *retrosolubility* phenomenon of perovskite, where its solubility decreases with increasing temperature.[18] This method allows the growth of high-quality perovskite single crystals, drastically reducing the synthesis time. However, the faster growth kinetics of ITC results in multiple nucleations and, hence, the formation of polycrystals, which overall affects the process reproducibility.[15] It has been claimed that the seed-assisted growth process, where a small seed crystal serves as the nucleation center for further growth,

Received: April 3, 2023
Revised: June 7, 2023
Published: July 5, 2023

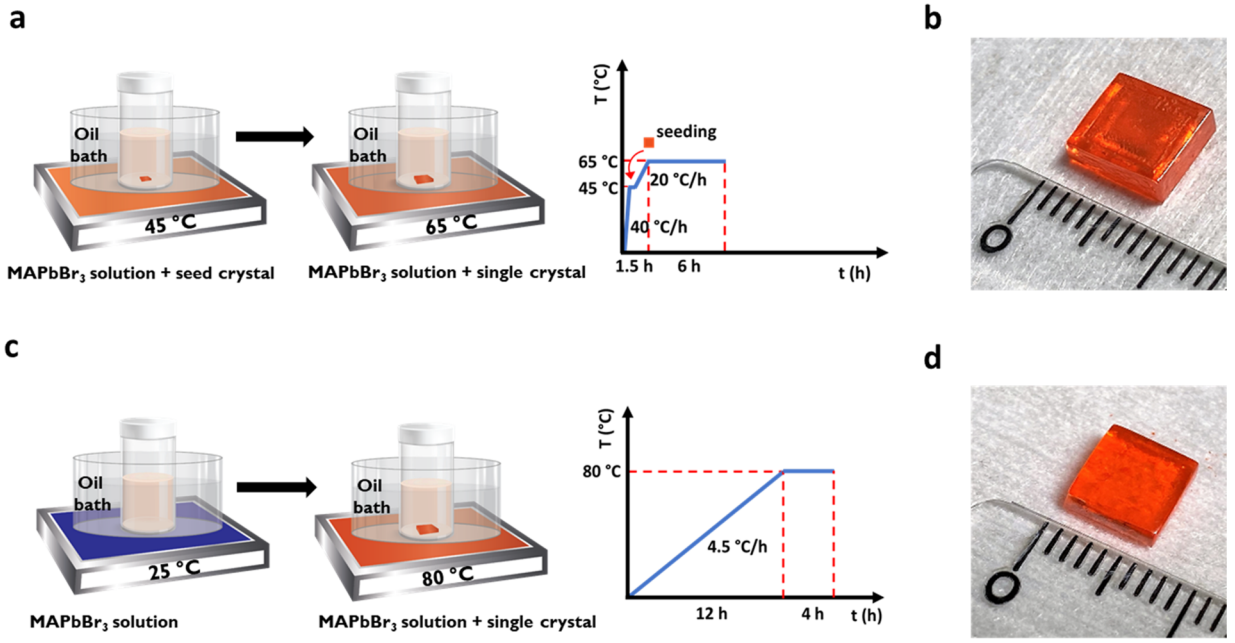

Figure 1. Schematics of $MAPbBr_3$ single crystal growth via the ITC method where perovskite precursor enclosed in a vial is placed in an oil bath on a heating plate. (a) Seed-assisted growth of $MAPbBr_3$ single crystal by two-step heating, first to 45 °C at a rate of 40 °C/h, where a seed crystal is introduced, and then the solution is heated to 65 °C/h at a rate of 20 °C/h and kept there for almost 6 h. (b) Photograph of a seeded $MAPbBr_3$ single crystal. (c) Nucleation-assisted growth of $MAPbBr_3$ single crystal by one step heating to 80 °C at a rate of 4.5 °C/h, and after nucleation the solution is kept at that temperature for almost 4 h. (d) Photograph of an unseeded $MAPbBr_3$ single crystal.

results in strain-free methylammonium lead bromide ($MAPbBr_3$) single crystals with improved process reproducibility. However, using this method, still the formation of polycrystals could not be inhibited completely because of the high temperature, i.e., 85 °C.[19] Seed-assisted growth has been widely employed in the literature as the method to grow larger single crystals. However, it has never been analyzed in depth how the seed-assisted growth method affects the final optoelectronic properties of the single crystal itself and as a photoconversion device compared to the ones grown via nucleation-assisted growth.[20,21] Interestingly, Sargent et al. have explored the seed-assisted growth for formamidinium lead iodide ($FAPbI_3$)-based thin film perovskite solar cells showing that the perovskite seed crystals embedded in the PbI_2 film act as nuclei to improve the crystallization during the perovskite formation. These films with seeded growth have shown lower trap density, resulting in highly efficient and stable solar cells with a power conversion efficiency of 21.5%.[22]

Here, we introduce a low-temperature seed-assisted ITC method for the growth of $MAPbBr_3$ single crystals. Based on this method, we have extensively analyzed the actual effects of the seed-assisted growth on the final optoelectronic properties of the $MAPbBr_3$ single crystals, in comparison with the nucleation-assisted method. We have demonstrated that it is possible to decrease the temperature established for the $MAPbBr_3$ growth until 65 °C, and still large, high-quality single crystals can be obtained in a short time, avoiding multiple nuclei formation. X-ray diffraction (XRD) analysis has revealed a lower crystal lattice strain for seeded crystals, confirming that the slower crystallization kinetics and directed growth via seeding result in high-quality single crystals compared with the nucleation-assisted crystals grown at a much higher temperature, i.e., 80 °C. Higher band-to-band radiative recombination is observed during steady-state photoluminescence (PL) analysis. A very low trap density in seeded single crystals is demonstrated by the space charge limited current (SCLC) method, confirming that the seed-assisted growth at a lower temperature helps to reduce the defects in the final crystal significantly. Further analysis by temperature-modulated SCLC (TM-SCLC) confirms these results, showing a higher trap energy level in the case of nucleation-assisted crystals. These differences are revealed as well in a final proof of concept for the application as photodetectors. The much higher responsivity of 5.49 A W^{-1} and detectivity values of 5.35×10^{11} jones for seeded crystals are obtained compared to unseeded single crystals having a responsivity and detectivity of 1.78 A W^{-1} and 4.64×10^{10} jones, respectively. These findings highlight how low-temperature kinetics during seed-assisted ITC can have a major impact on the final properties and applications, such as photodetectors.

2. RESULTS AND DISCUSSION

$MAPbBr_3$ single crystals with dimensions of 5−7 mm and 2 mm thickness were synthesized by the seed-assisted (seeded) and nucleation-assisted (unseeded) growth methods. For the seed-assisted growth, 1 M perovskite precursor solution in DMF was heated in the first step to a temperature of 45 °C at a ramp of 40 °C/h, and then a seed of $MAPbBr_3$ single crystal was introduced into that solution (see Figure 1a). (For the synthesis of seed crystals, see the Experimental Section). After the seed was introduced, the temperature was increased to 65 °C at a ramp of 20 °C/h in the second step, and the seed was kept growing for almost 6 h until the desired size was achieved, as shown in Figure 1b. For nucleation-assisted growth, the temperature of the 1 M $MAPbBr_3$ solution was increased in one step to 80 °C at a ramp of 4.5 °C/h, as shown in Figure 1c. After nucleation, the solution was kept at that temperature for about 4 h to grow unseeded single crystals of the same dimensions (Figure 1d). Comparing both protocols, it took

https://doi.org/10.1021/acs.chemmater.3c00780
Chem. Mater. 2023, 35, 5458−5467

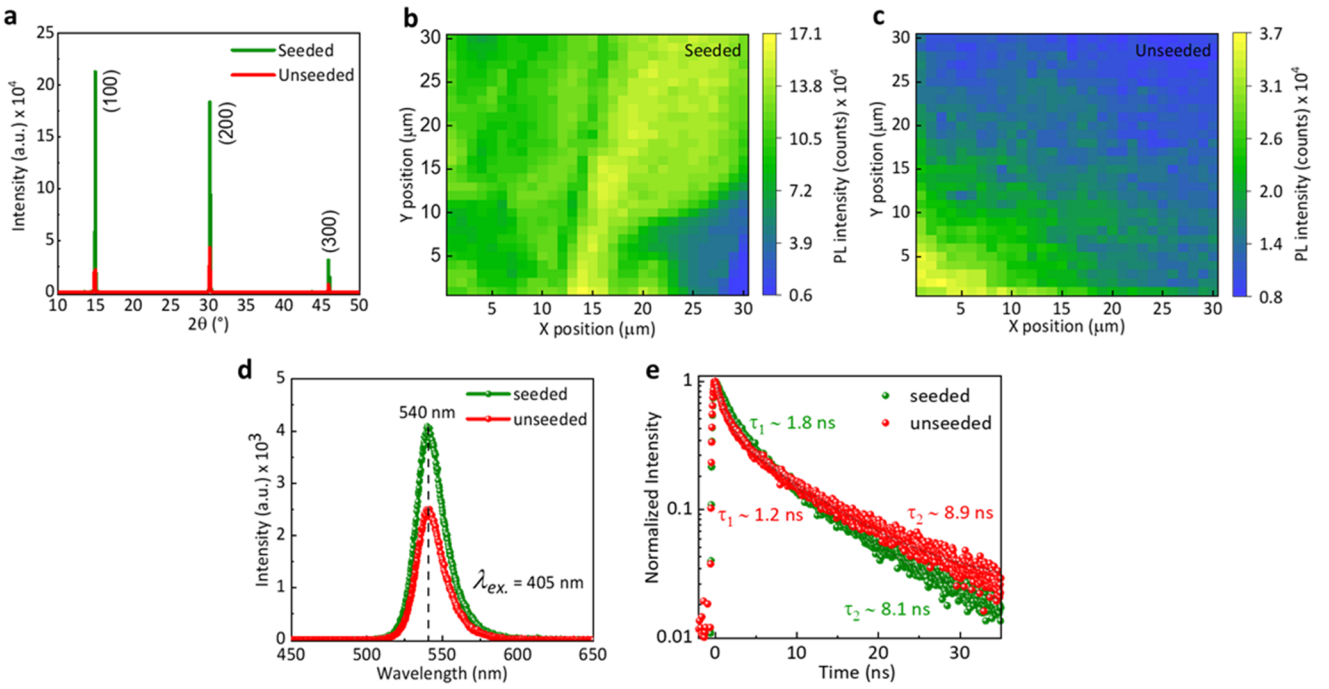

Figure 2. (a) XRD pattern of as-grown seeded (green) and unseeded (red) $MAPbBr_3$ single crystals. Spatially resolved PL mapping for (b) seeded and (c) unseeded single crystals. (d) Steady-state photoluminescence spectra of seeded and unseeded $MAPbBr_3$ single crystals measured at an excitation wavelength of 405 nm. (e) Transiently resolved photoluminescence.

almost 7.5 h to complete the whole process for seed-assisted growth and almost 16 h for nucleation-assisted growth.

It has been observed that in nucleation-assisted growth fast heating can cause multiple nucleation centers, leading to small crystallites that can lump together to produce polycrystals (Figure S2). The crystal growth in a solution system is mainly governed by the solute deposition rate on the crystal surface and the diffusion rate of the solute in the solution. A higher solute diffusion rate, as compared to the deposition rate, leads to an excess of solute precipitation in the form of many small crystallites and polycrystals. Keeping in mind the relationship between diffusion rate and the temperature[20]

$$D = D_0 \exp\left(-\frac{\Delta H}{RT}\right) \quad (1)$$

where D is the diffusion rate, D_0 is the diffusion constant, ΔH is the diffusion activation energy, R is the gas constant and T is the solution temperature. It is clear that in nucleation-assisted growth a constant high temperature of 80 °C for $MAPbBr_3$ increases the diffusion rate, resulting in crystal imperfections.[20] To avoid unnecessary nucleation and to have a good quality single crystal, the temperature should be controlled in such a way that a balance between the solute deposition rate and diffusion rate can be maintained. However, at a lower temperature, it is very challenging to overcome the nucleation energy for the formation of nuclei, which can later grow into larger crystals. The reason behind this is the low supersaturation of 1 M $MAPbBr_3$ solution at this lower temperature, which hinders the solute to crystallize. Liu et al. have reported that at a lower temperature of 60 °C nucleation-assisted ITC took over 2 weeks to reach sufficient supersaturation for nucleation and subsequent growth.[23]

This can be prevented with the help of seed-assisted growth. A small seed does not need to overcome the nucleation energy, as no supersaturation is needed to form a nucleus. Because a seed crystal itself is larger than the critical radius, it keeps on growing below the supersaturation limit. At a much lower temperature of 65 °C, the diffusion rate does not rise to a limit where extra solute results in further nucleation and thus the growth of multiple crystals simultaneously. With this approach, the reproducibility of the ITC method increases because no polycrystals are formed. Above all, a crystal of 5 mm × 5 mm with a thickness of 2 mm is achieved in just a few hours at a low-temperature profile (see Figure 1b).

To study the structural changes that occurred owing to the different growth protocols, XRD analysis is performed on seeded and unseeded $MAPbBr_3$ single crystals. Sharp and intense XRD reflections along (100), (200), and (300) planes confirm the formation of a highly crystalline perovskite cubic phase in seeded single crystals (see Figure 2a). However, for unseeded single crystals, an immense decrease of almost 100-fold in the XRD peak intensity has been observed, indicating lower crystallinity. In the case of unseeded growth, the overall crystallization kinetics are faster because of the higher temperature at 80 °C. As already mentioned, this leads to a much higher solute diffusion rate affecting the overall crystalline quality of the single crystals.[20] For seed-assisted growth, the seed crystal acts as a surface on which the dissolved solute can grow. This templated growth at a much lower temperature, i.e., 65 °C, helps to maintain a steady solute diffusion rate, yielding highly crystalline single crystals.[24]

The full width at half-maximum (FWHM) analysis of each reflection provides the lattice strain of both crystals using the tangent formula (details in the Experimental Section). As expected, higher FWHM has been calculated for unseeded single crystals which, consequently, leads to higher lattice strain within them. Table 1 summarizes the FWHM and lattice strain values of both seeded and unseeded single crystals.

These results follow the literature trend, where it was claimed that the nucleation-assisted grown (unseeded) single

https://doi.org/10.1021/acs.chemmater.3c00780
Chem. Mater. 2023, 35, 5458−5467

Table 1. FWHM Values and Calculated Lattice Strain Corresponding to Different XRD Reflections for Both Seeded and Unseeded Single Crystals

	FWHM (deg)		lattice strain (%)	
peak position 2θ (deg)	seeded	unseeded	seeded	unseeded
14.92	0.064	0.085	0.193	0.270
30.10	0.038	0.129	0.045	0.204
45.85	0.035	0.070	0.026	0.067

crystals have higher internal strain than the seeded ones.[19] Lattice strains, in turn, can accelerate ionic migration within the perovskite crystal, causing higher defect concentration and leading to nonradiative recombination processes.[25]

A sharp band edge was observed via steady-state absorption measurements for seeded and unseeded single crystals. Figure S3 reveals that no difference can be observed through the absorbance spectra in both cases. From their respective Tauc plots, the band gap value is the same, determined to be 2.19 eV, which is following the literature.[18]

The spatially resolved PL mapping shows a higher PL intensity with a more homogeneous distribution in the seeded crystal compared to the unseeded crystal (Figures 2b and 2c). This reconciles with the benefit of the seed-assisted method, promoting aligned growth with reduced bulk defects. The mapped area is further probed with steady-state PL and time-resolved PL (TRPL) measurements. The PL maxima are observed at 540 nm for both cases with no shift in the peak position (Figure 2d). The intensity for steady-state PL is higher for the seeded crystal, which is in accordance with PL mapping. These results further strengthen our findings from XRD analysis that the higher strain in the unseeded crystals is the cause of higher defect concentration, which consequently increases the nonradiative processes, quenching the PL response.

The TRPL measurement in Figure 2e shows two obvious features: a rapid decay within the first 3−5 ns, followed by an almost monoexponential slower decay. The fast decay (τ_1) corresponds to nonradiative recombination arising from the presence of a large number of surface defects. The lifetime τ_1 is 1.8 ns in the seeded as compared with 1.2 ns in the unseeded crystal. This improvement in lifetime is associated with a lower density of surface traps in seeded single crystals. As already mentioned, the seed crystal helps to direct the crystal growth limiting the uncoordinated species within the crystal lattice acting as traps for free carriers. The longer lifetime (τ_2) is associated with bulk radiative recombination. Lower τ_2 values in the case of seeded crystals primarily suggest a lower quality of the bulk. Alternatively, it may also be low due to the scattering from the different seeded interfaces. However, it is difficult to comment on the bulk behavior under low-energy excitation. Also, the excitation wavelength of 405 nm insufficiently excites the bulk. It is therefore more adequate to probe the bulk by two-photon absorption, i.e., $\lambda_{ex} > 800$ nm. In two-photon absorption, the penetration depth is close to the crystal thickness, where the generated charge carriers are homogeneously distributed throughout the crystals.[26]

The space charge limited current (SCLC) is a steady-state method used to analyze the charge transport properties of a semiconductor material by recording the dark current as a function of the applied voltage ($I-V$ curve measurements). In this technique, the defect states are probed with external charge carriers, and by doing that the defect density, their position within the band gap, and the charge carrier mobilities are determined. A typical SCLC trace consists of mainly three regimes, following the Mott−Gurney law for a sandwiched configuration: the Ohmic, the trap-filled limit (TFL), and the Child regime.[27] Both seeded and unseeded single crystals are characterized by the SCLC method to determine the trap densities in both cases.

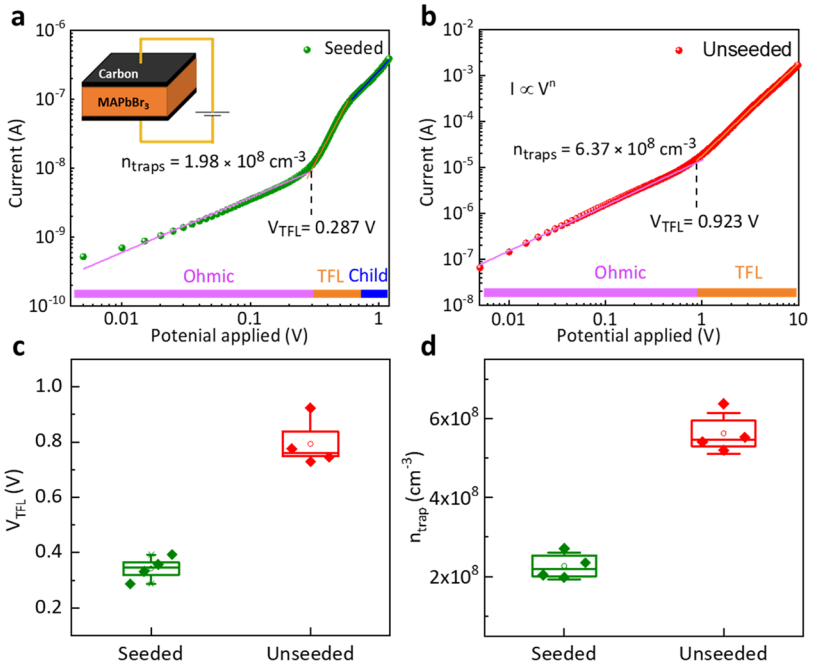

Figure 3. SCLC measurement curve with all the three regimes (i.e., Ohmic, traps filling limit (TFL), and Child regime) (a) for seeded $MAPbBr_3$ single crystals with a lower V_{TFL} = 0.287 V, (b) for unseeded $MAPbBr_3$ single crystals with a higher V_{TFL} = 0.923 V, (c) V_{TFL} statistics for 4 different $MAPbBr_3$ single crystals, and (d) density of traps (n_{trap}) statistics for 4 different $MAPbBr_3$ single crystals.

https://doi.org/10.1021/acs.chemmater.3c00780
Chem. Mater. 2023, 35, 5458−5467

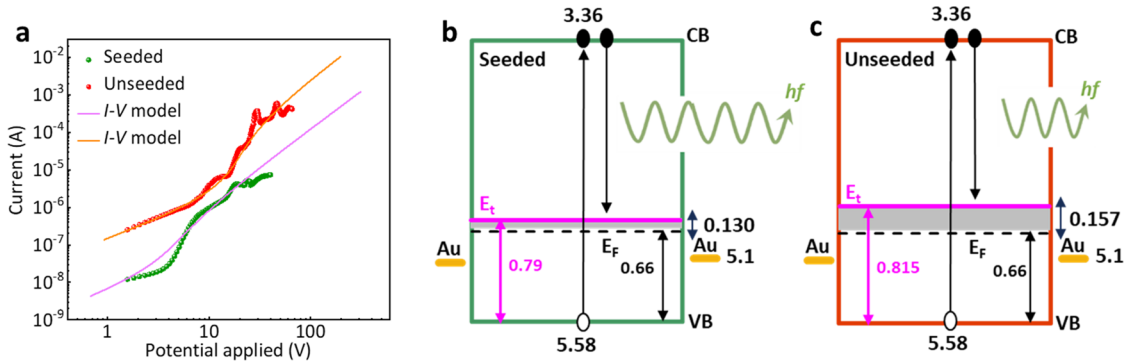

Figure 4. (a) TM-SCLC spectra for seeded and unseeded $MAPbBr_3$ single crystals (at an elevated temperature of 308.15 K). Solid lines represent the $I-V$ model consisting of a monoenergetic transport band and one monoenergetic trap to describe the experimental dependences of the concentration of free and trapped charge carriers for the studied perovskite. Schematic diagram of the energy levels illustrating the parameters obtained from the TM-SCLC method (b) for seeded $MAPbBr_3$ single crystals and (c) for unseeded $MAPbBr_3$ single crystals.

The differences in steady-state PL as well as in the TRPL analysis found for the seeded and unseeded crystals help us to predict significant changes in both trap densities and carrier mobilities. The higher-order pattern of the crystal lattice found for the seeded crystal must be associated with a reduced charge carrier trapping, favoring a longer diffusion length, which is proportional to the carrier mobility. Therefore, both types of single crystals with a thickness of 2 mm are sandwiched between two carbon electrodes deposited by the doctor-blade coating of carbon paste (see Figure S1) to perform SCLC analysis. A schematic of the device is shown in Figure 3a (inset). At lower bias, an Ohmic behavior ($I \propto V^{n=1}$) is observed, where the current increases linearly with the rise in applied bias. With further increase in the applied bias, there is a nonlinear increase in the current ($I \propto V^{n>3}$) providing evidence of a trap-filled limit.

This regime is governed by the onset voltage of the trap-filled limit regime (V_{TFL}). Here, almost all of the available traps are filled by the injected charge carriers. V_{TFL} is directly proportional to the density of traps n_{trap} given by the following equation:[28]

$$n_{trap} = \frac{V_{TFL}\varepsilon\varepsilon_0}{eL^2} \tag{2}$$

where ε_0 (8.85×10^{-12} F/m) represents the vacuum permittivity, ε_r the relative dielectric constant (ε_r = 25.5 for $MAPbBr_3$),[18] V_{TFL} the onset voltage of the trap-filled limit regime, e the charge of the electron (1.6×10^{-19} C), and L the thickness of the single crystal (2 mm). In the case of seeded single crystals, the trap-filled limit appears at V_{TFL} = 0.287 V, which is much lower than that for the unseeded single crystals at 0.923 V, as shown in Figures 3a and 3b. A lower V_{TFL} results in a lower trap density (n_{traps}), 1.98×10^8 cm^{-3}, for seeded crystals, unlike the unseeded ones with n_{traps} = 6.37×10^8 cm^{-3}. For seeded crystals, all traps are filled below 1 V, and the $I-V$ trace enters the trap-free Child regime where $I \propto V^{n=2}$. However, for unseeded crystals, the trap-filled limit was extended even until 10 V (see Figure 3b), and still no Child regime was obtained. Going beyond 10 V, which may harm the crystals and thus requires a careful revision of the current measurement setup, would be an important future avenue to further record the $I-V$ trace for unseeded single crystals. This limits the carrier mobility calculation. Higher trap density in unseeded $MAPbBr_3$ single crystals further complements the cause of the lower photoluminescence response. In addition to that, statistics are done by measuring $I-V$ traces (see Figure S4) for four different seeded and unseeded single crystals. As expected, all of the seeded crystals have shown quite lower V_{TFL} and, hence, lower trap densities as compared to that of unseeded single crystals, as shown in Figures 3c and 3d.

To confirm these results and further analyze the electronic characteristics of both crystals, we performed temperature-modulated SCLC (TM-SCLC) measurements. With this method, a quantitative evaluation of the density of trap states in the bandgap can be performed with higher energy resolution. Moreover, the determination of both the distribution of localized states (traps) and their energy can be evaluated due to the spectroscopic character of the method. The conditions for the measurement are completely set as previously published in ref 29 (see the Experimental Section for details). For these measurements, both seeded and unseeded $MAPbBr_3$ single crystals are sandwiched between thermally evaporated gold electrodes (further details in the Experimental Section). The data obtained with this method confirm the SCLC results discussed above, adding insights regarding the band gap rather than just the microscopic mobility and density of traps. In this way, the basic properties of perovskite single crystals can be determined from temperature-modulated current–voltage ($I-V$) characteristics (see Figure 4a).[29−31]

The dependence of drift mobility μ_d on the applied voltage V can be determined from current density $j = \frac{I}{S}$ (where S is the active area of a sandwiched crystal contact) using the equation[30]

$$\mu_d = \mu_0\Theta = \frac{jL^3}{\varepsilon_0\varepsilon_r(1-\gamma)(2-\gamma)^2V^2} \tag{3}$$

where μ_0 is the microscopic mobility (the mobility of free charge carriers in delocalized states), $m = \frac{1}{\gamma} = \frac{d\ln j}{d\ln V}$ is a slope of the $I-V$ trace (see Figure 4), L is the thickness of perovskite crystal, and the parameter Θ is defined as $\Theta = \frac{n_f}{n_f + n_t}$, where n_f is the concentration of free charge carriers and n_t is the concentration of trapped charge carriers. The parameter Θ = 1 for two cases: (a) when the material will be electrically neutral (i.e., Ohmic regime, n_t = 0) or (b) in Mott–Gurney's law (Child regime).

The microscopic mobility μ_0 (for seeded and unseeded crystals) is then estimated as the maximum drift mobility in the

https://doi.org/10.1021/acs.chemmater.3c00780
Chem. Mater. 2023, 35, 5458−5467

Table 2. Optoelectronic Properties of Seeded and Unseeded $MAPbBr_3$ Single Crystals Determined by TM-SCLC

	μ_0 ($m^2\ V^{-1}\ s^{-1}$)	$E_F - E_v$ (eV)	n_f (cm^{-3})	$E_t - E_v$ (eV)	$E_t - E_F$ (eV)	$n_t \approx N_t$ (cm^{-3})
seeded	0.03	0.66	2.39×10^8	0.790	0.130	9.47×10^9
unseeded	0.7	0.66	3.26×10^8	0.815	0.157	3.21×10^{10}

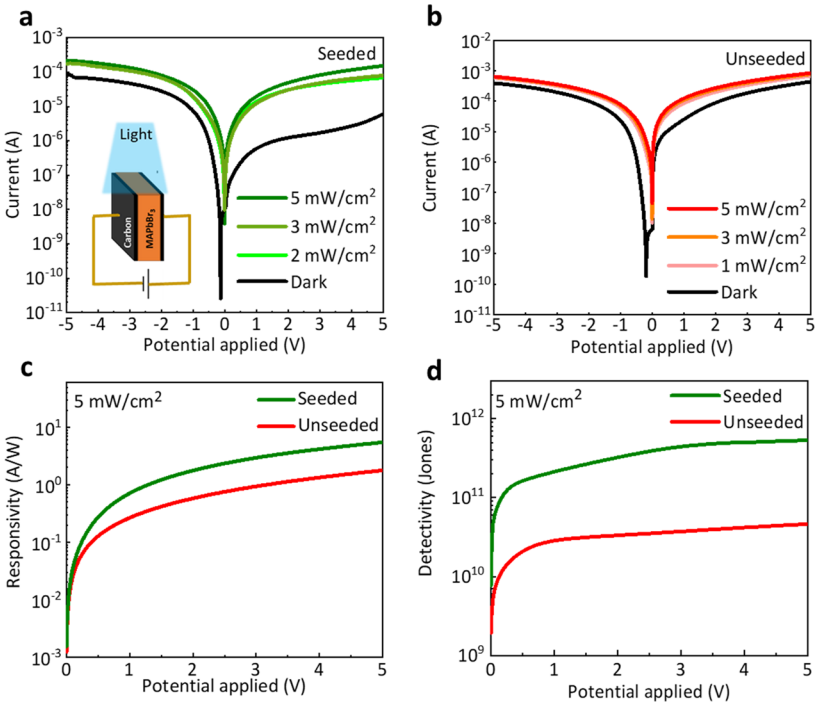

Figure 5. Dark and under-illumination $I-V$ curves at varying illumination intensities of 2, 3, and 5 mW cm^{-2} using a 473 nm LED light source. Applied bias goes from −5 to 5 V for $MAPbBr_3$ single crystals (a) seeded and (b) unseeded. (c, d) Responsivities and detectivities of seeded and unseeded single crystals at 5 mW cm^{-2} illumination intensity and a bias of 5 V.

Ohmic region and/or in the region where Mott−Gurney's law is valid. Subsequently, the concentration of free charge carriers n_f and trapped charge carriers n_t (on the applied voltage) are calculated (using the determined microscopic mobility) as follows:[30]

$$n_f = \frac{Lj}{e\mu_0(2-\gamma)V} \tag{4}$$

$$n_t = \frac{\varepsilon_0\varepsilon_r(1-\gamma)(2-\gamma)V}{eL^2} \tag{5}$$

Finally, the position of the Fermi's level (E_F) with respect to the valence band and the position of the trap states (E_t) with respect to the Fermi's level can be obtained using eqs 6 and 7, respectively:[30]

$$E_F - E_v = \frac{k_B T}{e} \ln\left(\frac{n_f}{N_v}\right) \tag{6}$$

$$E_F - E_t = \frac{k_B T}{e} \ln\left(\frac{n_t}{N_t}\right) \tag{7}$$

where T is the temperature (in kelvin), e is the electron charge, k_B is Boltzmann's constant, E_v is the energy of the valence band, $N_v = 2\sqrt{\frac{(2\pi m^* k_B T)^3}{h^6}}$ is the density of states in the valence band, h is Planck's constant, m^* is the effective mass of holes (for $MAPbBr_3$ is $\frac{m^*}{m_e} \approx 0.25$, where m_e is the mass of the electron),[32] and N_t is the density of electronic states (for thermal energies higher than $3k_BT$). In the Ohmic region, E_F can be rewritten as E_{F0}, corresponding to the position of Fermi's level in the thermodynamic equilibrium. All the determined parameters using TM-SCLC spectroscopy for both seeded ($L = 2.2 \times 10^{-3}$ m) and unseeded ($L = 2.0 \times 10^{-3}$ m) crystals with $T = 308.15$ K, $S = 9.0 \times 10^{-6}$ m^2, $\varepsilon_r = 25.5$, $E_c = -3.36$ eV, $E_v = -5.58$ eV, and $E_g = 2.22$ eV are summarized in Table 2.

As previously reported in ref 33, two factors must be considered when evaluating the energy levels of a system: the position of Fermi's level and the position of trap states, specifically the deep trap state. The determined parameters from TM-SCLC measurements are demonstrated through energy level diagrams of seeded and unseeded samples, as presented in Figures 4b,c. These band diagrams for both seeded and unseeded further strengthen our findings from steady-state PL. In the case of the unseeded single crystal, the trap state is at 0.157 eV with respect to Fermi's level, whereas for the seeded crystal, the trap state lies at an energy of 0.130 eV. This shows that the traps in the unseeded $MAPbBr_3$ single crystal are 25 meV higher as compared to the seeded crystal. Hence, a trap state at higher energy with respect to the Fermi's level may lead to higher nonradiative recombination, reducing photoluminescence response as in the case of unseeded single crystals (see Figure 4c). In addition to that, a lower trap density (n_t) of 9.47×10^9 cm^{-3} is calculated in seeded crystals, whereas unseeded $MAPbBr_3$ crystals have resulted in a higher n_t of 3.21×10^{10} cm^{-3}. The results obtained by TM-SCLC are

https://doi.org/10.1021/acs.chemmater.3c00780
Chem. Mater. 2023, 35, 5458−5467

in accordance with the SCLC calculations and further highlight the potential of seed-assisted growth, where one can achieve high-quality crystals with significantly reduced defect states. Another important aspect regarding the electrode material for these single crystalline devices has been observed. A similar trend in the trap densities with both carbon electrodes (for SCLC measurements) and gold electrodes (for TM-SCLC measurements) confirms the high reproducibility of the low-temperature seed-assisted growth for $MAPbBr_3$ crystals.

Vacancy-assisted ionic defects can act as traps for charge carriers in perovskite materials. Ionic diffusion results in the appearance of lattice defects, which have important implications for the long-term stability and performance of perovskite-based devices such as solar cells, LEDs, or photodetectors. Because of the difference in lattice strain and trap densities, both seeded and unseeded crystals are further characterized to study photodetector properties to comprehend the effect of their growth procedures when they interact with light of different optical powers. Photodetector sandwiched devices (see the inset of Figure 5a) are measured under varying illumination intensities of 2, 3, and 5 mW cm^{-2} using a 473 nm LED light source at an applied bias from −5 to 5 V. Figures 5a and 5b show $I-V$ curves under dark and illumination for both seeded and unseeded crystals, respectively.

The dark current in photodetectors arises due to the thermal excitation or generation of charge carriers caused by the defect states of lower ionization energy within the material. To have an efficient photodetector, dark currents should be as low as possible. Photodetectors with lower dark currents are favorable for detecting low optical powers.[34] As expected, a low dark current of I_{dark} of 6.01×10^{-6} A is observed in the seeded crystals, whereas a much higher I_{dark} of 4.36×10^{-4} A was recorded in the case of unseeded single crystals. Higher dark currents can be directly correlated to the presence of higher defects in unseeded single crystals. Furthermore (see Figures 5a and 5b), under an illumination intensity of 5 mW cm^{-2} the recorded photocurrent I_{ph} was 25.2 times higher than the I_{dark} in the case of seeded single crystals. Contrary to that, I_{ph} was only two times higher than that of I_{dark} for unseeded single crystals. As a result, higher responsivities and detectivities were obtained for the seeded crystals. Figures 5c and 5d show the responsivities and detectivities calculated at an increasing bias from 0 to 5 V, respectively. A seeded $MAPbBr_3$ single crystal has shown a maximum responsivity of 5.49 A W^{-1}, and in the case of an unseeded crystal, a responsivity value of 1.78 A W^{-1} was calculated at 5 V. Correspondingly, a higher detectivity value of 5.35×10^{11} jones was obtained for the seeded crystal, while the unseeded crystal showed 4.64×10^{10} jones. These findings confirm that $MAPbBr_3$ seeded crystals can be efficient photodetectors with lower dark currents compared with unseeded crystals.

3. CONCLUSION

In conclusion, we have demonstrated how differences in the growth method of perovskite single crystals can have a tremendous effect on their final optoelectronic properties. We have compared the conventional nucleation-assisted ITC versus a newly developed low-temperature seed-assisted ITC method for the growth of $MAPbBr_3$ single crystals. We have shown that the seed-assisted method helps to lower the crystal growth temperature from 80 to 65 °C, slowing down the overall growth kinetics of the ITC process. The result is higher crystallinity for the seeded crystals with a greatly reduced lattice strain. These less strained seeded $MAPbBr_3$ crystals have led to lower nonradiative recombination due to a significantly lower trap density, proved by the TM-SCLC method. The implication of these findings in direct technology as photodetectors is also proven, obtaining higher detectivity and responsivity responses for the seeded $MAPbBr_3$ crystals. These results highlight the importance of understanding and controlling the crystallization process of perovskite single crystals. A thorough analysis of the influence of the growth parameters on the final optoelectronic properties is essential to implement these materials as photodetectors at an industrial level, contributing as well to a better understanding of perovskite operation mechanisms.

4. EXPERIMENTAL SECTION

4.1. Materials and Reagents. Lead bromide (≥98%) was purchased from Sigma-Aldrich. *N*,*N*-Dimethylformamide DMF (extra dry, 99.8%) was purchased from Acros Organics. Methylammonium bromide (MABr) was purchased from Greatsolar (Australia). All salts and solvents were used as received without further purification. Carbon paste (DN-CP01) for contact was purchased from Dyenamo.

4.2. Synthesis of $MAPbBr_3$ Single Crystals. 1 M $MAPbBr_3$ precursor solution was prepared by dissolving MABr and $PbBr_2$ (1:1) in DMF. The powders were completely dissolved in the solvent by using a vortex shaker at room temperature. The solutions were further filtered using a 0.2 μm pore size PTFE filter. For nucleation-assisted growth, the solution was placed in an oil bath and slowly heated to 80 °C at a rate of 4.5 °C/h in one step. After nucleation, the single crystal was grown for approximately 4 h until it reached a size of approximately $5 \times 5 \times 2$ mm^3.

In the case of seeded growth, first, seed crystals were synthesized by heating the perovskite precursor solution to 80 °C for 1 h. When small crystals reached a size of approximately 1×1 mm^2, they were taken out of the solution and washed with DMF. Each seed crystal was carefully inspected under a magnifying glass to make sure that all dimensions are intact and that it is a high-quality seed crystal. For further growth, each seed crystal was then introduced to a separate vial of fresh 6 mL $MAPbBr_3$ precursor solution at a temperature of 45 °C. In the second step, the temperature of the precursor solution was then increased to 65 °C at a rate of 20 °C/h. The seed crystal was kept in the solution for approximately 6 h until it reached a size of approximately $5 \times 5 \times 2$ mm^3. In both cases, crystals were taken out of the solutions, rinsed with DMF, and then dried.

4.3. Fabrication of $MAPbBr_3$ Single Crystalline Devices. For SCLC measurements and photodetector characteristics, single crystalline devices were fabricated by depositing the carbon electrodes on both faces of $MAPbBr_3$ single crystals via doctor blade coating of carbon paste, as shown in Figure S1a. For TM-SCLC measurements, 100 nm gold electrodes of 2×2 mm^2 were deposited on both faces of single crystals by thermal evaporation (see Figure S1b).

4.4. Measurement and Characterization. The UV−vis spectra of the single crystals were measured with a PerkinElmer LAMBDA 1050. The lattice strain from XRD was calculated by using the Software Data Viewer from Malvern PANanalytical. The basis behind this calculation is the tangent formula:

$$\text{lattice strain} = \frac{B_{struct}}{4 \tan \theta}$$

B_{struct} describes the structural broadening, which is the difference in integral profile width between a standard (std) and the sample to be analyzed (obs):

$$B_{struct} = \sqrt{B_{obs}^{\ 2} - B_{std}^{\ 2}}$$

B_{obs} is the breadth obtained from the sample to be analyzed, and B_{std} is the breadth obtained from the standard sample, which does not exhibit any structural broadening effects.

https://doi.org/10.1021/acs.chemmater.3c00780
Chem. Mater. 2023, 35, 5458−5467

Micro-photoluminescence mapping was performed using a fiber-based scanning confocal microscope, with the samples placed in a vibration-free closed-cycle cryostat (AttoDRY800 from Attocube AG, with 50 × 50 μm^2 piezomotor scanners at RT). A continuous-wave (pulsed) excitation laser with a wavelength of λ = 405 nm was used to excite the sample, providing spectral and μ-TRPL measurements. Excitation and detection were performed using a 50X microscope objective with a long working distance and a numerical aperture of NA = 0.5, which was placed outside the cryostat. The sample emission was long-pass filtered, dispersed by a double 0.3 m focal length grating spectrograph (Acton SP-300i from Princeton Instruments), and detected with a cooled Si CCD camera (Newton EMCCD from ANDOR) for recording the μ-PL spectrum of a silicon single-photon avalanche photodiode detector APD (from Micro Photon Devices) connected to a time tagger (Time Tagger Ultra, from Swabian Instruments) for μ-TRPL measurements.

$I-V$ measurements for SCLC were performed using an Autolab GSTT302N potentiostat by applying a bias from 0 to 10 V in the dark in a face-to-face electrode configuration (C/$MAPbBr_3$/C). To check the reproducibility of the method, the same SCLC measurements were performed on four different $MAPbBr_3$ single crystals. According to ref 29, $I-V$ characteristics within the TM-SCLC measurements were performed using a voltage range from 0 to ∼50 V with a 1 mV step. The temperature was changed at the same time from 30 to 40 °C (5 min for both the heating and cooling process). The measurement took almost 2 days. For photodetector properties, illumination was done by using a SINUS-70 solar simulator comprising 21 LEDs of different wavelengths. The LED channel at 473 nm (green) was used to illuminate the single-crystal devices. The responsivity (R) and detectivity (D^*) at 5 mW/cm^2 were calculated using the following equations:

$$R = \frac{I_{ph} - I_{dark}}{P_{irra} S}; \qquad D^* = \frac{R}{(2eI_{dark})^{1/2}}$$

where I_{ph} is the photocurrent, I_{dark} is the dark current, P_{irra} is the power of the incident light intensity, S is the surface area of the crystals, and e is the electron charge (1.6×10^{-19} C).

■ ASSOCIATED CONTENT

Supporting Information

The Supporting Information is available free of charge at https://pubs.acs.org/doi/10.1021/acs.chemmater.3c00780.

Photographs of $MAPbBr_3$ single crystalline devices sandwiched between carbon and gold electrodes, photographs of $MAPbBr_3$ polycrystals formed at 80 °C, UV−vis and SCLC plots (PDF)

■ AUTHOR INFORMATION

Corresponding Authors

Clara A. Aranda − *Institute for Photovoltaics (ipv), University of Stuttgart, 70569 Stuttgart, Germany; IEK-5 Photovoltaics, Forschungszentrum Jülich, 52425 Jülich, Germany*; Email: clara.alonso@ipv.uni-stuttgart.de

Michael Saliba − *Institute for Photovoltaics (ipv), University of Stuttgart, 70569 Stuttgart, Germany; IEK-5 Photovoltaics, Forschungszentrum Jülich, 52425 Jülich, Germany*; orcid.org/0000-0002-6818-9781; Email: michael.saliba@ipv.uni-stuttgart.de

Authors

Waqas Zia − *Institute for Photovoltaics (ipv), University of Stuttgart, 70569 Stuttgart, Germany; IEK-5 Photovoltaics, Forschungszentrum Jülich, 52425 Jülich, Germany*

Jan Pospisil − *Materials Research Centre, Faculty of Chemistry, Brno University of Technology, 612 00 Brno, Czech Republic*

Alexander Kovalenko − *Department of Applied Mathematics, Faculty of Information Technology, Czech Technical University in Prague, 160 00 Brno, Czech Republic*

Monika Rai − *Institute for Photovoltaics (ipv), University of Stuttgart, 70569 Stuttgart, Germany*; orcid.org/0000-0002-7173-3370

Cristina Momblona − *Instituto de Ciencia de los Materiales (ICMUV), Universidad de Valencia, 46980 Paterna, Valencia, Spain*

Setatira Gorji − *Instituto de Ciencia de los Materiales (ICMUV), Universidad de Valencia, 46980 Paterna, Valencia, Spain*

Guillermo Muñoz-Matutano − *Instituto de Ciencia de los Materiales (ICMUV), Universidad de Valencia, 46980 Paterna, Valencia, Spain*; orcid.org/0000-0002-8178-0808

Complete contact information is available at: https://pubs.acs.org/10.1021/acs.chemmater.3c00780

Author Contributions

W.Z. grew single crystals and performed and analyzed the UV−vis, SCLC, and photodetector measurements. W.Z. wrote the first draft of the manuscript with the supervision of C.A.A. and M.S. All authors contributed to the discussion, commented, reviewed and approved the paper. C.A.A. and M.S. developed the original idea and co-designed the experimental and characterization plan together with W.Z. J.P. and A.K. performed TM-SCLC measurements and analyzed the results. M.R. analyzed the PL and TRPL data and helped in writing that part. C.M. performed the XRD measurements and helped with the analysis. S.G. and G.M.M. performed the PL and TRPL measurements. M.S. directed, guided and supervised the research.

Notes

The authors declare no competing financial interest.

■ ACKNOWLEDGMENTS

M.S., W.Z., and C.A.A. thank the Helmholtz Young Investigator Group FRONTRUNNER. M.S. thanks the German Research Foundation (DFG) for funding (SPP2196, 431314977/GRK 2642). M.S. acknowledges funding by ProperPhotoMile. Project ProperPhotoMile is supported under the umbrella of SOLARERA.NET cofunded by The Spanish Ministry of Science and Education and the AEI under Project PCI2020-112185 and CDTI Project IDI-20210171; the Federal Ministry for Economic Affairs and Energy based on a decision by the German Bundestag Projects FKZ 03EE1070B and FKZ 03EE1070A and the Israel Ministry of Energy with Project 220-11-031. SOLAR-ERA.NET is supported by the European Commission within the EU Framework Programme for Research and Innovation HORIZON 2020 (Cofund ERA-NET action number 786483) funded by the European Union. M.S. acknowledges funding from the European Research Council under the Horizon Europe program (LOCAL-HEAT, Grant Agreement 101041809). M.S. acknowledges funding from the German Bundesministerium für Bildung and Forschung (BMBF), project "NETPEC" (01LS2103E). M.R. thanks the Alexander von Humboldt Foundation for the research fellowship. C.M. acknowledges the funding from the "Contratación de personal investigador doctor con experiencia internacional CDEIGENT" (ref CDEIGENT/2021/022) from the Consellería de Innovación, Universidades, Ciencia y

https://doi.org/10.1021/acs.chemmater.3c00780
Chem. Mater. 2023, 35, 5458−5467

Sociedad Digital de la Generalitat Valenciana, Spain. G.M.M. thanks the Ramón y Cajal program (Contract RYC2020-030099-I) and the 2D-SPD (Two-Dimensional Semiconductor Photonic Dots) project, funded by the Spanish Ministry of Science MICINN, AEI (RTI2018-099015-J-I00), and the European Regional Development Fund (ERDF). C.A.A. acknowledges the support from the Margarita Salas Post-doctoral Contract MGS/2022/25(UP2021-021) financed by the European Union-Next Generation EU. W.Z. thanks Vladimir Chivrony for the support in PL measurements. W.Z. thanks Mayank Kedia and Shama Perween for the scientific discussions.

REFERENCES

(1) Kim, M.; Kim, G.-H.; Lee, T. K.; Choi, I. W.; Choi, H. W.; Jo, Y.; Yoon, Y. J.; Kim, J. W.; Lee, J.; Huh, D.; Lee, H.; Kwak, S. K.; Kim, J. Y.; Kim, D. S. Methylammonium Chloride Induces Intermediate Phase Stabilization for Efficient Perovskite Solar Cells. *Joule* **2019**, *3*, 2179−2192.

(2) Best Research-Cell Efficiencies: Emerging Photovoltaics, NREL, https://www.nrel.gov/pv/cell-efficiency.html (accessed 2023-06).

(3) Tan, Z.-K.; Moghaddam, R. S.; Lai, M. L.; Docampo, P.; Higler, R.; Deschler, F.; Price, M.; Sadhanala, A.; Pazos, L. M.; Credgington, D.; Hanusch, F.; Bein, T.; Snaith, H. J.; Friend, R. H. Bright light-emitting diodes based on organometal halide perovskite. *Nat. Nanotechnol.* **2014**, *9*, 687−692.

(4) Li, C.; Wang, H.; Wang, F.; Li, T.; Xu, M.; Wang, H.; Wang, Z.; Zhan, X.; Hu, W.; Shen, L. Ultrafast and broadband photodetectors based on a perovskite/organic bulk heterojunction for large-dynamic-range imaging. *Light. Sci. Appl.* **2020**, *9*, 31.

(5) Stranks, S. D.; Eperon, G. E.; Grancini, G.; Menelaou, C.; Alcocer, M. J. P.; Leijtens, T.; Herz, L. M.; Petrozza, A.; Snaith, H. J. Electron-hole diffusion lengths exceeding 1 micrometer in an organometal trihalide perovskite absorber. *Science* **2013**, *342*, 341−344.

(6) Shi, D.; Adinolfi, V.; Comin, R.; Yuan, M.; Alarousu, E.; Buin, A.; Chen, Y.; Hoogland, S.; Rothenberger, A.; Katsiev, K.; Losovyj, Y.; Zhang, X.; Dowben, P. A.; Mohammed, O. F.; Sargent, E. H.; Bakr, O. M. Solar cells. Low trap-state density and long carrier diffusion in organolead trihalide perovskite single crystals. *Science* **2015**, *347*, 519−522.

(7) Lian, Z.; Yan, Q.; Gao, T.; Ding, J.; Lv, Q.; Ning, C.; Li, Q.; Sun, J.-L. Perovskite CH3NH3PbI3(Cl) Single Crystals: Rapid Solution Growth, Unparalleled Crystalline Quality, and Low Trap Density toward 10^8 cm^{-3}. *J. Am. Chem. Soc.* **2016**, *138*, 9409−9412.

(8) Wang, Q.; Zhang, G.; Zhang, H.; Duan, Y.; Yin, Z.; Huang, Y. High-Resolution, Flexible, and Full-Color Perovskite Image Photodetector via Electrohydrodynamic Printing of Ionic-Liquid-Based Ink. *Adv. Funct. Mater.* **2021**, *31*, 2100857.

(9) Li, L.; Ye, S.; Qu, J.; Zhou, F.; Song, J.; Shen, G. Recent Advances in Perovskite Photodetectors for Image Sensing. *Small* **2021**, *17*, e2005606.

(10) Huang, X.; Guo, Y.; Liu, Y. Perovskite photodetectors and their application in artificial photonic synapses. *Chem. Commun.* **2021**, *57*, 11429−11442.

(11) Jokar, E.; Cai, L.; Han, J.; Nacpil, E. J. C.; Jeon, I. Emerging Opportunities in Lead-Free and Lead−Tin Perovskites for Environmentally Viable Photodetector Applications. *Chem. Mater.* **2023**, *35*, 3404−3426.

(12) Zhou, J.; Luo, J.; Rong, X.; Wei, P.; Molokeev, M. S.; Huang, Y.; Zhao, J.; Liu, Q.; Zhang, X.; Tang, J.; Xia, Z. Lead-Free Perovskite Derivative Cs_2SnCl_{6-x} Br_x Single Crystals for Narrowband Photodetectors. *Adv. Optical Mater.* **2019**, *7*, 1900139.

(13) Ma, N.; Jiang, J.; Zhao, Y.; He, L.; Ma, Y.; Wang, H.; Zhang, L.; Shan, C.; Shen, L.; Hu, W. Stable and sensitive tin-lead perovskite photodetectors enabled by azobenzene derivative for near-infrared acousto-optic conversion communications. *Nano Energy* **2021**, *86*, 106113.

(14) Feng, A.; Jiang, X.; Zhang, X.; Zheng, X.; Zheng, W.; Mohammed, O. F.; Chen, Z.; Bakr, O. M. Shape Control of Metal Halide Perovskite Single Crystals: From Bulk to Nanoscale. *Chem. Mater.* **2020**, *32*, 7602−7617.

(15) Lian, Z.; Yan, Q.; Gao, T.; Ding, J.; Lv, Q.; Ning, C.; Li, Q.; Sun, J.-L. Perovskite $CH_3NH_3PbI_3(Cl)$ Single Crystals: Rapid Solution Growth, Unparalleled Crystalline Quality, and Low Trap Density toward 10^8 cm^{-3}. *J. Am. Chem. Soc.* **2016**, *138*, 9409−9412.

(16) Saidaminov, M. I.; Adinolfi, V.; Comin, R.; Abdelhady, A. L.; Peng, W.; Dursun, I.; Yuan, M.; Hoogland, S.; Sargent, E. H.; Bakr, O. M. Planar-integrated single-crystalline perovskite photodetectors. *Nat. Commun.* **2015**, *6*, 8724.

(17) Lee, L.; Baek, J.; Park, K. S.; Lee, Y.-E.; Shrestha, N. K.; Sung, M. M. Wafer-scale single-crystal perovskite patterned thin films based on geometrically-confined lateral crystal growth. *Nat. Commun.* **2017**, *8*, 15882.

(18) Saidaminov, M. I.; Abdelhady, A. L.; Murali, B.; Alarousu, E.; Burlakov, V. M.; Peng, W.; Dursun, I.; Wang, L.; He, Y.; Maculan, G.; Goriely, A.; Wu, T.; Mohammed, O. F.; Bakr, O. M. High-quality bulk hybrid perovskite single crystals within minutes by inverse temperature crystallization. *Nat. Commun.* **2015**, *6*, 7586.

(19) Amari, S.; Verilhac, J.-M.; Gros D'Aillon, E.; Ibanez, A.; Zaccaro, J. Optimization of the Growth Conditions for High Quality $CH_3NH_3PbBr_3$ Hybrid Perovskite Single Crystals. *Cryst. Growth Des.* **2020**, *20*, 1665−1672.

(20) Liu, Y.; Zhang, Y.; Yang, Z.; Feng, J.; Xu, Z.; Li, Q.; Hu, M.; Ye, H.; Zhang, X.; Liu, M.; Zhao, K.; Liu, S. Low-temperature-gradient crystallization for multi-inch high-quality perovskite single crystals for record performance photodetectors. *Mater. Today* **2019**, *22*, 67−75.

(21) Rakita, Y.; Kedem, N.; Gupta, S.; Sadhanala, A.; Kalchenko, V.; Böhm, M. L.; Kulbak, M.; Friend, R. H.; Cahen, D.; Hodes, G. Low-Temperature Solution-Grown $CsPbBr_3$ Single Crystals and Their Characterization. *Cryst. Growth Des.* **2016**, *16*, 5717−5725.

(22) Zhao, Y.; Tan, H.; Yuan, H.; Yang, Z.; Fan, J. Z.; Kim, J.; Voznyy, O.; Gong, X.; Quan, L. N.; Tan, C. S.; Hofkens, J.; Yu, D.; Zhao, Q.; Sargent, E. H. Perovskite seeding growth of formamidinium-lead-iodide-based perovskites for efficient and stable solar cells. *Nat. Commun.* **2018**, *9*, 1607.

(23) Liu, Y.; Zhang, Y.; Zhao, K.; Yang, Z.; Feng, J.; Zhang, X.; Wang, K.; Meng, L.; Ye, H.; Liu, M.; Liu, S. F. A 1300 mm^2 Ultrahigh-Performance Digital Imaging Assembly using High-Quality Perovskite Single Crystals. *Adv. Mater.* **2018**, *30*, 1707314.

(24) He, J.; Wang, S.; Li, X.; Zhang, F. Seeding Agents in Metal Halide Perovskite Solar Cells: From Material to Mechanism. *ChemSusChem* **2023**, *16*, e202202109.

(25) Jones, T. W.; Osherov, A.; Alsari, M.; Sponseller, M.; Duck, B. C.; Jung, Y.-K.; Settens, C.; Niroui, F.; Brenes, R.; Stan, C. V.; Li, Y.; Abdi-Jalebi, M.; Tamura, N.; Macdonald, J. E.; Burghammer, M.; Friend, R. H.; Bulović, V.; Walsh, A.; Wilson, G. J.; Lilliu, S.; Stranks, S. D. Lattice strain causes non-radiative losses in halide perovskites. *Energy Environ. Sci.* **2019**, *12*, 596−606.

(26) Bi, Y.; Hutter, E. M.; Fang, Y.; Dong, Q.; Huang, J.; Savenije, T. J. Charge Carrier Lifetimes Exceeding 15 s in Methylammonium Lead Iodide Single Crystals. *J. Phys. Chem. Lett.* **2016**, *7*, 923−928.

(27) Duijnstee, E. A.; Ball, J. M.; Le Corre, V. M.; Koster, L. J. A.; Snaith, H. J.; Lim, J. Toward Understanding Space-Charge Limited Current Measurements on Metal Halide Perovskites. *ACS Energy Lett.* **2020**, *5*, 376−384.

(28) Liu, Y.; Zhang, Y.; Zhao, K.; Yang, Z.; Feng, J.; Zhang, X.; Wang, K.; Meng, L.; Ye, H.; Liu, M.; Liu, S. F. A 1300 mm^2 Ultrahigh-Performance Digital Imaging Assembly using High-Quality Perovskite Single Crystals. *Adv. Mater.* **2018**, e1707314.

(29) Pospisil, J.; Zmeskal, O.; Nespurek, S.; Krajcovic, J.; Weiter, M.; Kovalenko, A. Density of bulk trap states of hybrid lead halide perovskite single crystals: temperature modulated space-charge-limited-currents. *Sci. Rep.* **2019**, *9*, 3332.

(30) Zmeskal, O.; Nespurek, S.; Weiter, M. Space-charge-limited currents: An E-infinity Cantorian approach. *Chaos, Solitons & Fractals* **2007**, *34*, 143−158.

https://doi.org/10.1021/acs.chemmater.3c00780
Chem. Mater. 2023, 35, 5458−5467

(31) Gavranovic, S.; Blahut, J.; Zmeskal, O.; Pospisil, J.; Zhivkov, I. Charge density in MAPbBr3 perovskite: Application of thermomodulated SCLC. In *Thermophysics 2021:26th International Meeting of Thermophysics 2021*; AIP Publishing: 2022; p 20006.
(32) Zu, F.; Amsalem, P.; Egger, D. A.; Wang, R.; Wolff, C. M.; Fang, H.; Loi, M. A.; Neher, D.; Kronik, L.; Duhm, S.; Koch, N. Constructing the Electronic Structure of $CH_3NH_3PbI_3$ and $CH_3NH_3PbBr_3$ Perovskite Thin Films from Single-Crystal Band Structure Measurements. *J. Phys. Chem. Lett.* **2019**, *10*, 601−609.
(33) Gavranovic, S.; Pospisil, J.; Zmeskal, O.; Novak, V.; Vanysek, P.; Castkova, K.; Cihlar, J.; Weiter, M. Electrode Spacing as a Determinant of the Output Performance of Planar-Type Photodetectors Based on Methylammonium Lead Bromide Perovskite Single Crystals. *ACS Appl. Mater. Interfaces* **2022**, *14*, 20159−20167.
(34) Sutherland, B. R.; Johnston, A. K.; Ip, A. H.; Xu, J.; Adinolfi, V.; Kanjanaboos, P.; Sargent, E. H. Sensitive, Fast, and Stable Perovskite Photodetectors Exploiting Interface Engineering. *ACS Photonics* **2015**, *2*, 1117−1123.

https://doi.org/10.1021/acs.chemmater.3c00780
Chem. Mater. 2023, 35, 5458−5467